Creep of single-crystals of nickel-base γ-alloy at temperatures between 1150 °C and 1288 °C

Alexander I. Epishin, Bernard Fedelich, Bernard Viguier, Sina Schriever, Igor L. Svetlov, Nikolay V. Petrushin, Romain Saillard, Arnaud Proietti, Dominique Poquillon, Anton Chyrkin

Creep of single-crystals of nickel-base γ-alloy at temperatures between 1150 °C and 1288 °C

A.I. Epishin [a], B. Fedelich [b,*], B. Viguier [c], S. Schriever [b], I.L. Svetlov [d], N.V. Petrushin [d], R. Saillard [c], A. Proietti [c], D. Poquillon [c], A. Chyrkin [e]

[a] Institute for Materials Science and Technology, Technical University of Berlin, Berlin, Ernst-Reuter-Platz 1, 10587, Germany
[b] Federal Institute for Materials Research and Testing (BAM), Unter den Eichen 87, 12205, Berlin, Germany
[c] CIRIMAT, Université de Toulouse, CNRS, INP-ENSIACET, 4 allée Emile Monso, BP 44362, 31030, Toulouse cedex 4, France
[d] All-Russian Institute of Aviation Materials (VIAM), Radio Str. 17, 105005, Moscow, Russia
[e] Chalmers University of Technology, Kemivagen 10, 412 96, Gothenburg, Sweden

ARTICLE INFO

Keywords:
Nickel alloys
Single-crystals
Creep
Electron microscopy
Deformation mechanisms

ABSTRACT

A γ-analogue of the superalloy CMSX-4 that does not contain the strengthening γ′-phase and only consists of the γ-solid solution of nickel has been designed, solidified as single-crystals of different orientations, and tested under creep conditions in the temperature range between 1150 and 1288 °C. The tests have revealed a very high creep anisotropy of this alloy, as was previously found for CMSX-4 at supersolvus temperature of 1288 °C. This creep anisotropy could be explained by the dominance of ⟨011⟩{111} octahedral slip. Furthermore, the analysis of the creep data has yielded a high value of the creep activation energy, $Q_c \approx 442$ kJ/mol, which correlates with the high activation energy of Re diffusion in Ni. This supports the hypothesis that dislocation motion in the γ-matrix of Re-containing superalloys is controlled by the diffusion of the Re atoms segregating at the dislocation core. The Norton stress exponent n is close to 5, which is a typical value for pure metals and their alloys. The absence of γ′-reprecipitation after high-temperature creep tests facilitates microstructural investigations. It has been shown by EBSD that creep deformation results in an increasing misorientation of the existing low angle boundaries. In addition, according to TEM, new low angle boundaries appear due to reactions of the $a/2$ ⟨011⟩ mobile dislocations and knitting of new networks.

1. Introduction

In order to remove the microporosity, single-crystal blades cast of nickel-base superalloys are subjected to hot isostatic pressing (HIP) in a narrow temperature range between the γ′-solvus and the solidus temperatures [1–5]. Since the strengthening γ′- precipitates are totally dissolved, the blade material is very soft at these supersolvus temperatures. For example, the company Howmet Alcoa, USA, performs HIP for single-crystal blades of the nickel-base superalloy CMSX-4 at 1288 °C. This temperature is slightly above the γ′-solvus temperature of this alloy but below its solidus temperature, respectively equal to 1282 °C and 1339 °C [6]. However, HIPing the costly single-crystal blades at such high temperatures can damage them by recrystallization or incipient melting. Therefore, the parameters of commercial HIP (temperature T, pressure p, duration t) have to be carefully optimized to ensure full pore healing, while avoiding material damage and keeping processing costs low.

The HIP parameters could be optimized by using a physical model considering the mechanisms of porosity annihilation during HIP. One possible mechanism is pore closure via dislocation motion, as modeled in Refs. [3,4]. Therefore, in order to support HIP modeling, the creep behavior of superalloys at supersolvus temperatures has to be investigated. In a previous work [7], we investigated creep of CMSX-4 at 1288 °C. However, two experimental problems were encountered:

- First, the supersolvus temperature range in which CMSX-4 can be mechanically tested (1282–1339 °C) is too narrow for a reliable measurement of the temperature dependence of the creep rate of this alloy as a γ-solid solution. Moreover, the mechanical testing of CMSX-4 close to its solidus temperature is technically difficult because it bears the risk of incipient melting of the tested material. This makes it impossible to determine the creep activation energy Q_c,

* Corresponding author. Bundesanstalt für Materialforschung und -prüfung, Germany.
E-mail address: bernard.fedelich@bam.de (B. Fedelich).

https://doi.org/10.1016/j.msea.2021.141880

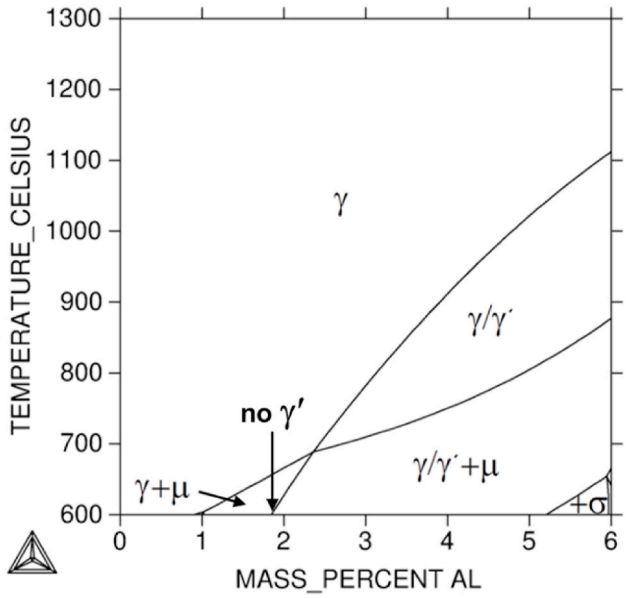

Fig. 1. Al–Ni section of the phase diagram of CMSX-4 (Ti and Ta are removed) calculated by the software Thermo-Calc.

Table 1
Composition of CMSX-4, and planned and cast γ-alloy, at%.

Alloy	Base	γ′-formers			γ-stabilizers				
	Ni	Al	Ti	Ta	Cr	Co	Mo	W	Re
CMSX-4	63.7	12.6	1.3	2.1	7.6	9.3	0.4	2	1
γ-alloy as planned	77	4	0	0	7	9	0	2	1
γ-alloy as cast	77.6	3.6	0	0	7.1	8.8	0	1.9	1

which is an important physical parameter related to the creep mechanism.

- Second, the γ′-phase reprecipitates during the cooling following the creep tests, which alters the dislocation structure and hinders the identification of the deformation mechanisms by Transmission Electron Microscopy (TEM).

To solve these problems, a model alloy compositionally similar to CMSX-4 but structurally free of the strengthening γ′-phase has been designed in this work. The alloy has been solidified as single crystals of different orientations, tested under creep conditions in the temperature range between 1150 °C and 1288 °C, and investigated by electron microscopy. The investigations aimed at understanding the creep behavior of the γ-solid solution of nickel at very high temperatures.

2. Experimental

The investigated model alloy is a γ-analogue of the nickel-base superalloy CMSX-4® [8], which is widely used in the gas turbine industry and in aero-engines as blade material. In the following, we will refer to this model alloy as the "γ-alloy". It has been designed under the two following conditions:

- First, the alloy should be compositionally similar to CMSX-4 but structurally free of the strengthening γ′-phase in the entire temperature range.
- Second, its creep resistance at temperatures above the γ′-solvus temperature of CMSX-4 (1282 °C) should be close to the creep resistance of CMSX-4; that is, at these temperatures the degree of its solid solution strengthening should be comparable to CMSX-4.

Therefore, as compared to CMSX-4, the content of γ′-formers (Al, Ti, Ta) in the γ-alloy has been significantly reduced while the content of the main solid solution strengtheners (Cr, Co, W, Re) has been maintained at the same level. Ti and Ta have been completely eliminated while the Al content has been decreased down to a level where no γ′-precipitation occurs. Fig. 1 shows the Al–Ni section of the phase diagram of CMSX-4 (Ti and Ta are removed) calculated with Thermo-Calc [9] using the thermodynamic database for Ni-based alloys TTNi7 [10]. It can be seen that the alloy is γ′-free at Al concentrations below 1.85 wt% (4.15 at%). Accordingly, the content Al was reduced to 4 at%. For the sake of simplicity, Mo, which concentration in CMSX-4 is only 0.38 at%, has been removed. Additionally, Mo has a negative effect on oxidation resistance, which is important for high-temperature creep tests.

A small sample with the planned composition (see "γ-alloy planned" in Table 1) and a weight of about 20 g has been cast by induction levitation melting and investigated in a TEM as well as by differential scanning calorimetry (DSC). The TEM analysis has shown no γ′-precipitates in dark-field images (see Fig. 2a) as well as no superlattice reflections from the γ′-phase in electron diffraction patterns (see Fig. 2b). The shape of the measured DSC curve (Fig. 3) has confirmed the absence of γ′-precipitation: No characteristic γ′-peaks are observed during heating and subsequent cooling. The DSC analysis has given the values 1430 °C and 1475 °C for the solidus and liquidus temperatures, respectively. These values have been used to select the thermal conditions for the solidification of the γ-alloy specimens.

Single-crystals of the γ-alloy have been manufactured at the All-Russian Institute of Aviation Materials (VIAM) Moscow, Russia. The master alloy of the planned composition has been alloyed in a vacuum induction furnace at a temperature between 1550 °C and 1570 °C with a hold time of about 10 min. The composition of the cast alloy has been checked by atomic emission spectroscopy. The results are presented in Table 1, see "γ-alloy as cast". It is seen that the concentrations of the alloying elements in the cast alloy are close to the planned ones.

Single-crystals of axial orientations [001], [011], [123] and [111] (middle of a stereographic triangle) have been directionally solidified by the Bridgman method in the furnace UNVK-9A VIAM having a liquid metal cooling system (cooling in liquid aluminum). The different orientations have been obtained by seeds placed in the crucible bottom, thereby enabling a selection of the crystal growth direction. The obtained single-crystal bars were cylinders of diameter 15 mm and length 170 mm. After solidification, the bars have been subjected to a two-step homogenization heat treatment under vacuum, 2 h at 1285 °C and 18 h at 1320 °C, followed by cooling at 60 °C/min down to 1000 °C. The orientations of the cylinders' axes have been measured by X-ray diffraction (XRD) and the results are graphically presented in Fig. 4. It can be seen that the orientations of the solidified single-crystals are close to the exact orientations [001], [011], [123] and [111].

Cylindrical creep specimens of 8 mm diameter and 115 mm total length have been machined from these bars and tested in air under tensile creep conditions according to ISO 204. The tests have been carried out in constant load arm machines, equipped by resistive ATS-furnaces with SiC heating elements operating at temperatures up to 1500 °C. These furnaces have a short hot zone of about 75 mm. However, within the gage length of 25 mm, the temperature field is quite uniform. Indeed, temperature measurements have shown that the difference between the center and the ends of the gage length is less than 5 °C. The longitudinal creep strain has been measured within this 25 mm gage length with an axial MTS-extensometer protected from radiation by a water-cooled shield, which allows to use it up to 1450 °C. Note that all the measuring equipment has been calibrated.

The first creep test carried out with an uncoated specimen of γ-alloy at 1288 °C has shown strong oxidation after a short testing time. Such an oxidation behavior is very different from the CMSX-4, which demonstrated a good oxidation resistance at this temperature [7]. Obviously, the reason for this difference is the much lower Al content in the γ-alloy, which protects the material at high temperatures by forming an alumina

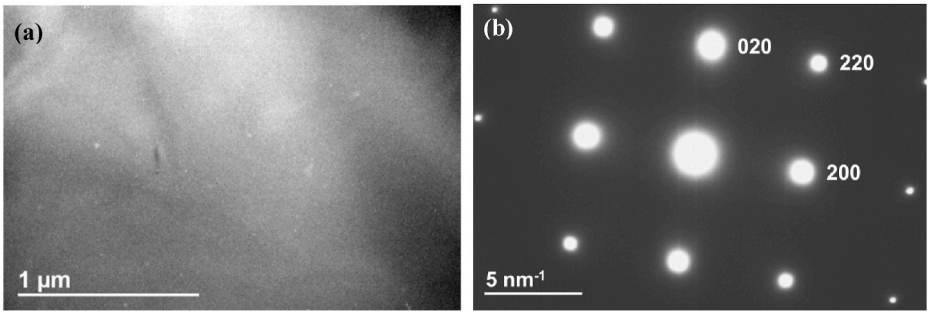

Fig. 2. TEM confirmation of the single-phase γ-structure of designed alloy. (a) Dark-field image. (b) Selected area electron diffraction pattern.

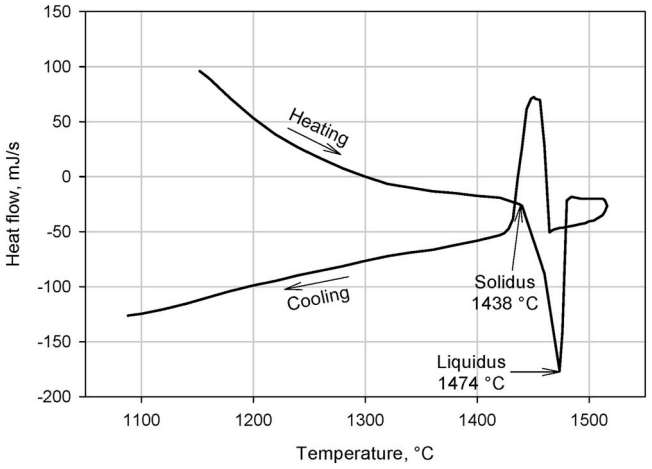

Fig. 3. DSC curves of γ-alloy measured in helium with heating/cooling rates ±20 °C/min.

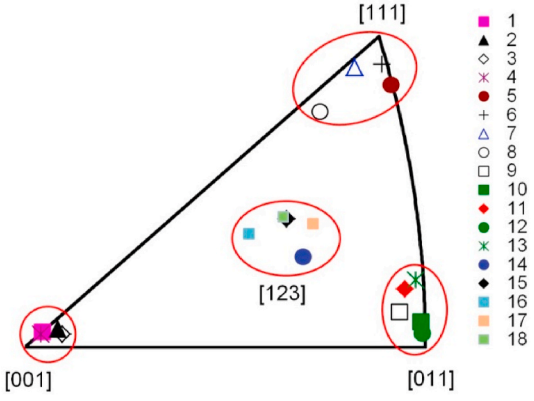

Fig. 4. Distribution of the axial orientations of the γ-alloy single-crystals in the standard stereographic triangle.

scale. Therefore, the remaining specimens have been coated by a 50 μm thick NiCoCrAlY–Ta protective layer sputtered using the HP – HVOF (high pressure – high velocity oxygen fuel) technique.

In order to determine the creep activation energy Q_c, specimens have been tested at three temperatures, 1150 °C, 1225 °C and 1288 °C (the last one is the CMSX-4 HIP temperature) for each orientation. Most of the tests have been performed under the stress of 10 MPa, which allowed fitting Q_c independently from the stress exponent n of Norton creep law. In addition, a few specimens have been tested at 1225 °C under different stress levels, i.e., 6 and 13 MPa, to enable the estimation of the stress exponent n at this temperature. Most of the tests have been interrupted at creep strains between 5 and 10 % for subsequent microstructural investigations. In order to "freeze" the dislocation structure, the specimens have been rapidly cooled down by air-jet under load. In the temperature interval 1288 °C → 400 °C, the cooling rate was about 15 °C/s.

After testing, the specimens have been investigated by different methods aiming at the identification of the deformation mechanisms at 1288 °C. In order to identify the active slip systems, the cross-section shape of one [011] specimen tested at 1288 °C has been characterized in an optical microscope, as described in Ref. [7]. Electron microscopy characterization has been performed at the Raimond Castaing Microanalysis Center (Toulouse, France). Scanning Electron Microscopy (SEM) and Electron Back Scattered Diffraction (EBSD) analysis have been carried out in order to follow the evolution of subgrain structure during high temperature creep tests. A Jeol JSM 7100F microscope equipped with an Oxford EBSD system has been used. The samples have been mechanically ground and then electrolytically polished before observations. The dislocation structures have been inspected by TEM, using a Jeol JEM 2100F apparatus. A classical electropolishing process has been conducted for thin foil preparation. Note that in order to get access to a large number of diffraction vectors, the foils have been cut along a (101) plane, i.e., inclined 45° off the load axis.

3. Results

3.1. Analysis of the creep curves

The creep curves of the [001], [011], [123], and [111] specimens of the γ-alloy are presented in Fig. 5 by solid lines. Fig. 5a–c shows the creep curves obtained under the stress of 10 MPa but at different temperatures, i.e., at 1150 °C, 1225 °C, and 1288 °C. At all temperatures, a pronounced creep anisotropy is observed. The highest creep resistance is shown by the [111] orientation and the lowest by the [001] orientation. The [011] and [123] single-crystals have an intermediate creep resistance with a slightly higher strength of the [011] orientation with respect to [123]. It is also seen that the creep rate is strongly temperature-dependent, as shown by the different time scales of the creep curves in Fig. 5a–c obtained at 1150 °C, 1225 °C, 1288 °C, and 10 MPa. It is also strongly stress-dependent, as demonstrated by the creep curves in Fig. 5d obtained at 1225 °C for the stress levels 6, 10, and 13 MPa.

A similar creep anisotropy was observed for CMSX-4 in Ref. [7] and explained by octahedral slip ⟨011⟩{111}. In Fig. 5a, the creep curves of the γ-alloy (solid lines) are compared with the corresponding creep curves of CMSX-4 (dashed lines). It follows that at 1288 °C the creep resistance of the γ-alloy is in the same order of magnitude as that of CMSX-4, but the CMSX-4 is noteworthily stronger. To characterize the difference in creep resistance, the average strain rate between 0 and 5 % has been considered. The corresponding ratios for the γ-alloy to CMSX-4, i.e. $\dot{\varepsilon}^{\gamma}_{av}(0 \quad 5\%)/\dot{\varepsilon}^{CMSX-4}_{av}(0 \quad 5\%)$, range from 1.4 for [111] to 2.6 for [011], with an average value of about 2 for all orientations.

The shapes of the creep curves of CMSX-4 and the γ-alloy are noticeably different. The creep curves of CMSX-4 have a quasi-

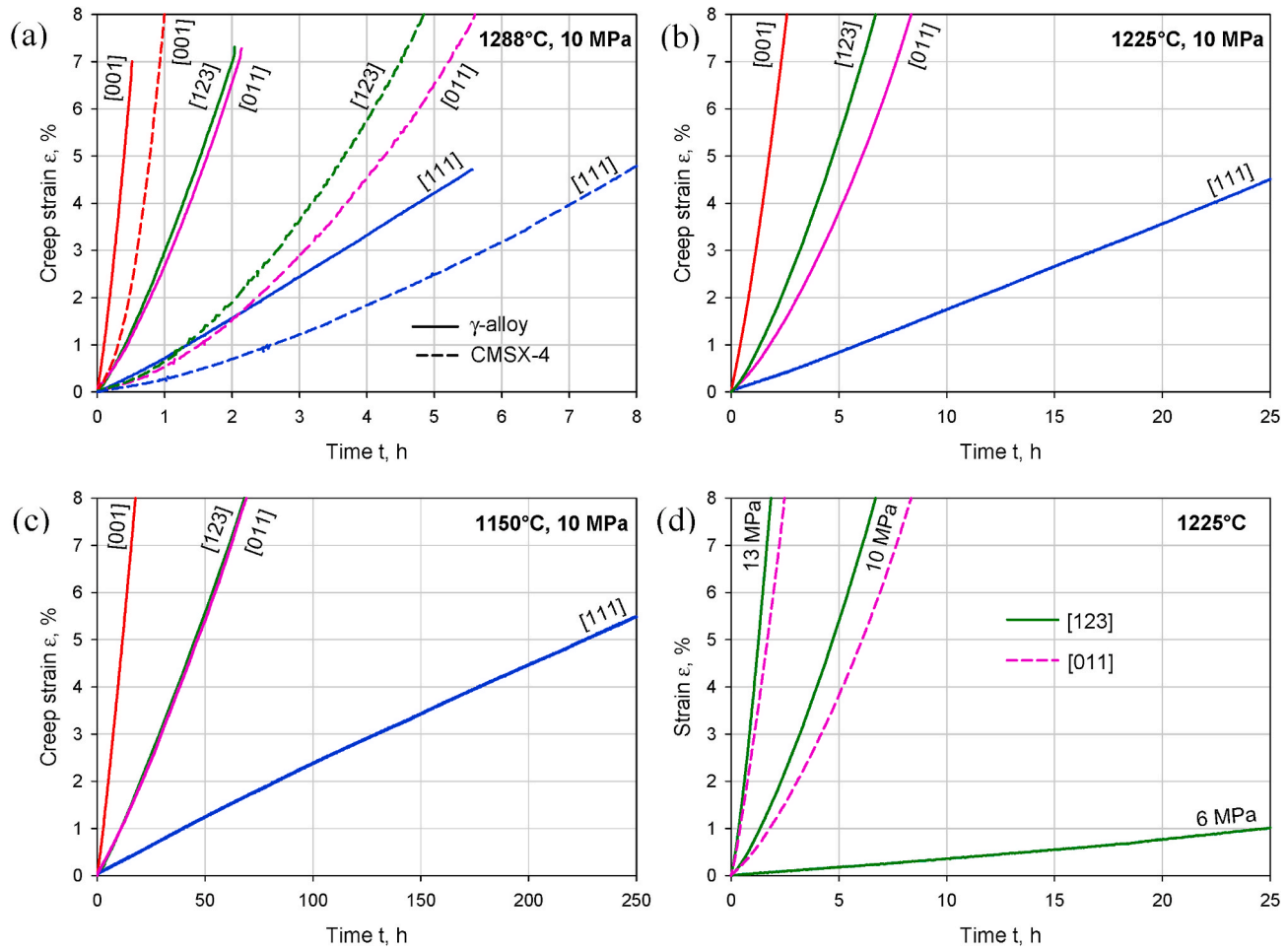

Fig. 5. Creep curves of γ-alloy single-crystals of different orientations at 1288 °C (a), 1225 °C (b, d), and 1150 °C (c). (a–c) Different temperatures but the same stress of 10 MPa. (d) Temperature of 1225 °C but different stresses, 6, 10, and 13 MPa. (a) Comparison of γ-alloy with CMSX-4 at 1288 °C and 10 MPa.

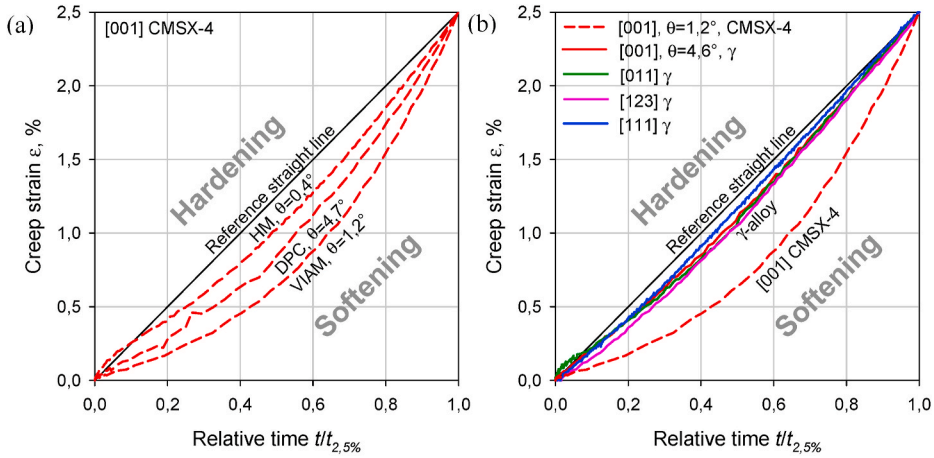

Fig. 6. Creep strain vs. normalized time $t/t_{2.5\%}$, 1288 °C, and 10 MPa. (a) [001] CMSX-4 crystals from different producers, VIAM, DPC, and HM. The deviations θ from the [001] ideal orientation are given in the graph. (b) Comparison between the γ-alloy and CMSX-4. The solid lines correspond to γ-alloy crystals of different orientations, the dashed line to a [001] CMSX-4 specimen.

exponential shape, with an accelerating creep rate from the beginning indicating softening. In contrast, the creep curves of the γ-alloy are almost straight, which indicates that creep occurs without significant softening or hardening. However, it is difficult to compare the softening behavior of these two materials based on the creep curves presented in Fig. 5a, because the CMSX-4 and the γ-alloy single-crystals have been produced by different companies, respectively, by Doncasters Precision Castings (DPC) Bochum, Germany, and by VIAM Moscow, Russia, and the solidification conditions differ.

Indeed, as can be observed in Fig. 6a for the CMSX-4 at 1288 °C, the softening behavior of CMSX-4 single-crystals supplied by different producers significantly differs. Fig. 6a compares the creep results of [001]

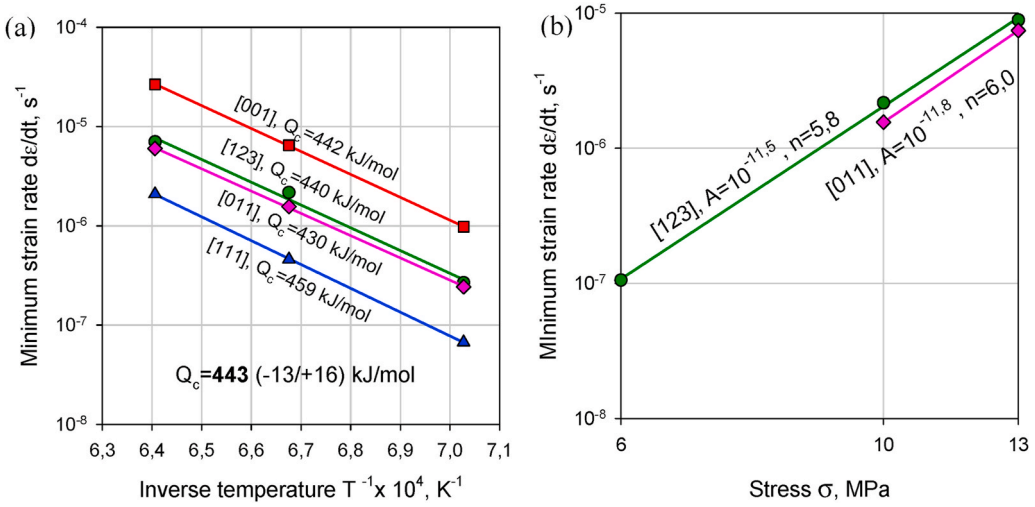

Fig. 7. Evaluation of the creep activation energy Q_c and the stress exponent n of the γ-alloy by the separated fitting of different orientations. (a) Fitting of Q_c for the creep tests at 1150 °C, 1225 °C, 1288 °C and the stress level 10 MPa. (b) Fitting of n for the creep tests at 1225 °C and stresses 6, 10, and 13 MPa.

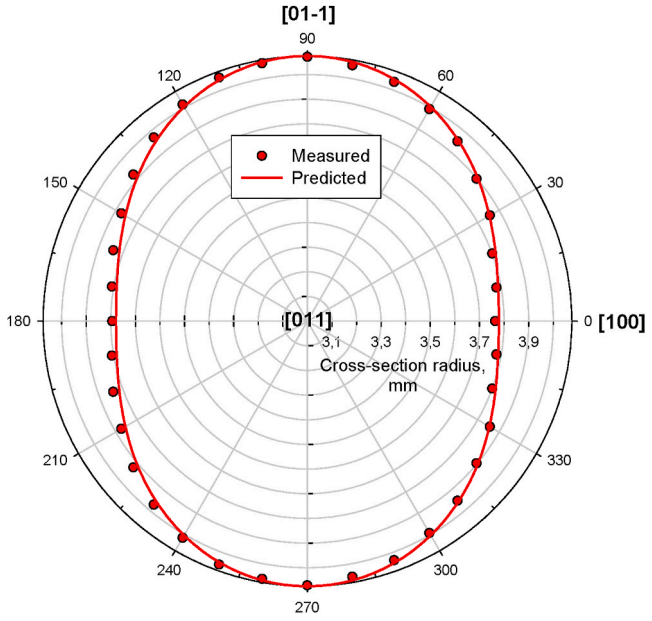

Fig. 8. Shape of the cross-section of a [011] specimen of the γ-alloy tested at 1288 °C, 10 MPa. The test has been interrupted at the creep strain of 7.3 %. The red dots and the elliptical red curve are respectively the experimental results and the theoretical prediction assuming ⟨011⟩{111} octahedral slip. (For interpretation of the references to colour in this figure legend, the reader is referred to the Web version of this article.)

single-crystals of CMSX-4 supplied by VIAM, DPC, and Howmet (HM) Alcoa, USA. The softening behavior is emphasized by plotting the creep strain as a function of the normalized time $t/t_{2.5\%}$, where $t_{2.5\%}$ is the time to reach the creep strain ε 2.5 %. Despite the smallness of the orientation differences (θ within 0.4–4.7°), the specimens exhibit a significantly different softening behavior. The most pronounced softening is shown by the VIAM specimen, followed by the DPC, and finally the HM specimen. In this regard, it should be noted that the specimens produced by VIAM have been solidified by liquid metal cooling (LMC), while the specimens received from DPC and HM by radiation cooling. In the same order, the primary dendrite arm spacing λ_{PDA}, characterizing the density of the dendritic structure of these specimens, takes values of about 210, 280, and 360 μm, which correlates with the different solidification rates. According to the results of investigations performed at the VIAM, the creep behavior of single-crystal superalloys is significantly influenced by their subgrain structure, which is more developed in the single-crystals grown under high-temperature gradient as in the case of the LMC method.

Among the available results for CMSX-4 in our group, only one [001] specimen tested at 1288 °C under 10 MPa can be directly used for comparison with the γ-alloy. Indeed, this CMSX-4 single-crystal and the γ-alloy crystals have been grown in the furnace UNVK-9A of VIAM under similar LMC solidification conditions. The comparison between this specimen and γ-alloy specimens of several orientations is presented in Fig. 6b in the same way as in Fig. 6a. First, irrespective of their orientations, the normalized creep curves $\varepsilon^{\gamma}_{hkl}$ $f(t/t_{2.5})$ of the γ-specimens are almost identical and straight, pointing to the absence of softening or hardening. On the opposite, the CMSX-4 creep curve $\varepsilon^{CMSX-4}_{hkl}$ $f(t/t_{2.5})$ shows significant softening indicated by a pronounced creep rate acceleration.

All creep curves of the γ-alloy have been analyzed and the minimum strain rates $\dot{\varepsilon}_{min}$ determined in order to identify the creep activation energy Q_c and the stress exponent n of Norton's creep law. In this section, Q_c and n have been evaluated by a simple linear regression of the creep rates separately for each orientation. A global fitting of an anisotropic Norton-type creep model with all test results requires an analytical description of the creep rate anisotropy, $\dot{\varepsilon}_{min}$ $f(\theta,\rho)$, where θ and ρ are the Euler angles characterizing the specimen orientation. Such an approach will be presented below in the Discussion section. The value of Q_c has been evaluated by linear fitting of the Arrhenius plots, assuming that $\dot{\varepsilon}_{min} \sim exp(\quad Q_c/RT)$, where R is the universal gas constant and T is the absolute temperature.

The Arrhenius plots in Fig. 7a summarize the results for the [001], [011], [123] and [111] specimens tested at the temperatures 1150 °C, 1225 °C, and 1288 °C, and at the same stress of 10 MPa (see the corresponding creep curves in Fig. 5a–c). The experimental results are well approximated by straight lines. The trend lines corresponding to different orientations are vertically shifted due to the different creep resistances but have nearly the same slope. The linear regressions give close Q_c values for the different orientations, respectively 442, 430, 440, and 459 kJ/mol for [001], [011], [123], and [111], with an average value of 443 (13/+16) kJ/mol. The stress exponent n has been evaluated with the results obtained for the [011] and [123] specimens tested at the same temperature of 1225 °C but under different applied stresses σ: 6, 10, and 13 MPa (see the corresponding creep curves in Fig. 5d). Fig. 7b shows the fitting results assuming a power-law i.e., $\dot{\varepsilon}_{min} \sim \sigma^n$. The line of best fit for [011] is slightly shifted down with respect to that for [123],

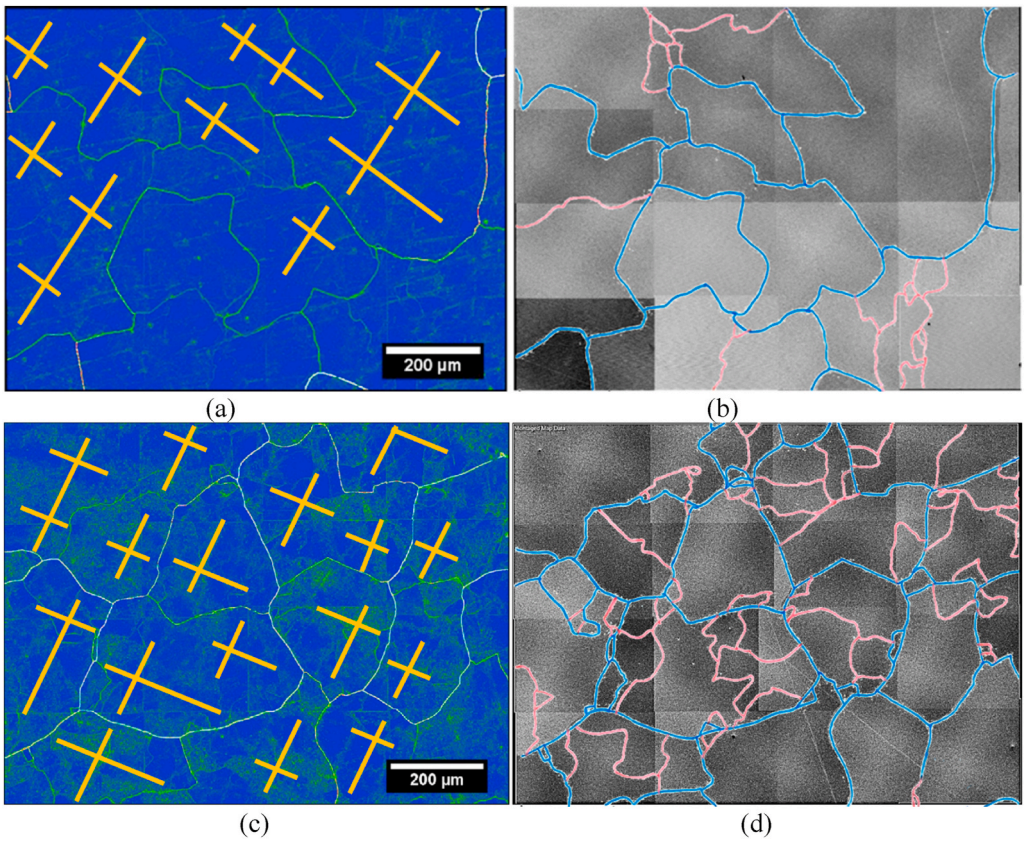

Fig. 9. Comparison of the subgrain structure of [001] specimens of γ-alloy before (a, b) and after (c, d) creep at 1288 °C, 10 MPa and 7 % creep strain. EBSD analysis with KAM mapping (a,c) and scattered electrons images (b,d). See text for details.

reflecting the fact that the [011] orientation is a little stronger. The trend lines are nearly parallel, with slopes yielding close values for the stress exponent, $n \approx 6.0$ for [011] and $n \approx 5.8$ for [123]. Due to the small number of data points on the graph $\dot{\varepsilon}_{min}$ $f(\sigma)$, these values should be only considered as a preliminary estimate of n. A more refined analysis, taking into account the whole experimental data, will be given below in the Discussion section.

3.2. Investigation of the shape of a deformed cross-section

The previous section has shown that the creep anisotropy of the γ-alloy observed in this work is similar to that reported in Ref. [7] for CMSX-4 at 1288 °C, for which the main creep mechanism was identified as octahedral slip ⟨011⟩{111}. Another evidence for the operation of octahedral slip could be obtained from the analysis of the deformed cross-section of a [011] specimen after an interrupted creep test, as shown in Ref. [7]. Therefore, the same analysis has been performed for a [011] specimen of γ-alloy deformed at 1288 °C under 10 MPa. The test has been interrupted after 2.1 h at an accumulated creep strain of 7.3 %. The measured values of the cross-section radius are plotted in Fig. 8 (dots) as a function of the azimuthal angle measured counterclockwise from the [001] direction. The shape of the deformed cross-section, as calculated by the large strain formalism in Ref. [7], and assuming that the material deforms by octahedral slip only is an ellipse, with its major axis along $[01\bar{1}]$ and its minor axis along [001]. The eccentricity of the ellipse is directly related to the longitudinal creep strain ε 7.3 %. The measurements agree very well with the elliptical shape predicted under the assumption of octahedral slip.

It was shown in Ref. [7] that octahedral slip is the only mechanism that leads to the observed elliptical cross-section. Other potential creep mechanisms like ⟨011⟩{100} cubic slip [11,12] or ⟨011⟩{011} climb [13–15] also lead to an elliptical shape of the cross-section, but rotated by 90°; that is, with the major axis along [100]. Creep controlled by bulk diffusion (Nabarro-Herring model [16,17]) isotropically reduces the specimen cross-section without changing its shape; that is, the cross-section remains circular.

3.3. SEM & TEM investigations

A few specimens of the γ-alloy have been selected for investigations in SEM by EBSD and in TEM. Fig. 9 shows the comparison of the subgrain structure of [001] specimens before (a, b) and after (c, d) creep at 1288 °C, 10 MPa and 7 % creep strain. Low angle boundaries (LABs) are highlighted in the Kernel Average Misorientation (KAM) mapping (a, c) deduced from EBSD analysis of both specimens. Some LABs have a clearly higher degree of misorientation, others lower. It is known that two types of LABs exist in single-crystals of nickel-base superalloys: interdendritic LABs (highlighted in blue in Fig. 9b and d) between the dendritic subgrains with misorientation up to a few degrees and intradendritic LABs (highlighted in red in Fig. 9b and d) located inside the dendritic subgrains and separating the mosaic blocks, which misorientation is one order of magnitude lower [6,18].

To unambiguously distinguish these two types of LABs, the dendrites have been identified through the density contrast of scattered electron images taken in EBSD mode using a Forward Scatter Detector (FSD). They are marked by crosses in Fig. 9a, c. The visible LABs in the EBSD map of the undeformed specimen (Fig. 9a) are mainly interdendritic, while in the map of the deformed specimen (Fig. 9c) numerous intradendritic LABs can be observed in addition. Schematic drawings of these LABs have been reported in the FSD images in Fig. 9b, d. The misorientations of these LABs have been measured and it appears that they increase after creep: the mean misorientation of interdendritic LABs is 0.62° before creep and 1.11° after creep. Note that the misorientations of intradendritic LABs in undeformed specimens (typically ~0.1° [18])

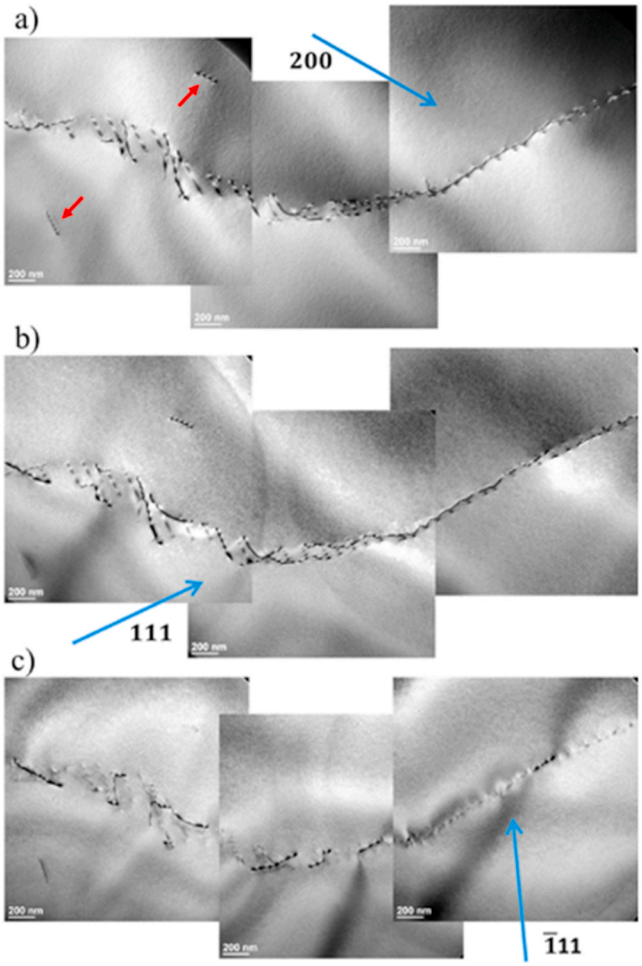

Fig. 10. Overview of the area near a LAB in a [001] specimen tested at 1288 °C, 10 MPa up to 7 % creep strain. Bright field two-beam TEM micrographs, the diffraction vector is indicated.

are below the angular resolution of the EBSD method and therefore such LABs cannot be seen in Fig. 9a. However, intradendritic LABs become visible after creep, with a mean misorientation below 0.5°, which clearly indicates dislocation activity within the subgrains. During creep, dislocations crossing the subgrains can either be arrested by reacting with the dislocations of preexisting intradendritic LABs, leading to an increase of their misorientation, or react one with each other, thereby knitting new LAB networks.

The SEM observations have been confirmed by TEM analysis of dislocation structure. Fig. 10, which shows a LAB with its surrounding area, is an example of TEM observation for the same deformed specimen as in Fig. 9. The LAB mesh size is about 100 nm, from which the misorientation can be estimated as about 0.1–0.2°. Thus, it is presumably an intradendritic LAB. As a striking feature of these TEM observations, although several images have been taken under different diffraction conditions, only very few dislocations could be observed inside the cells limited by such LABs. In Fig. 10a one can observe only two short individual segments (marked by red arrows), which were nearly the only ones visible in the cell interior. All in all, the dislocation landscape mainly consists of dislocation networks forming LABs and delimiting cells, the interior of which is nearly free from dislocations. What might be surprising at first glance can be understood from a theoretical estimate of the density of mobile dislocations ρ_m.

The assumption of dislocation motion controlled by the diffusion of solute atoms leads to high velocities at 1288 °C, for which the density ρ_m of the mobile dislocations required to sustain the creep rate according to the Orowan equation is low. For an applied stress of 10 MPa, the Orowan equation leads to the estimate $\rho_m \approx 0.8\ \mu m^{-2}$ (see Appendix). The area of TEM image in Fig. 10 is about 10 μm^2. Therefore, taking the TEM foil thickness as 0.1 μm, we get the analyzed volume, $V \approx 1\ \mu m^3$. Multiplying ρ_m by V gives the dislocation line length that is expected to be contained in the analyzed volume as $L \quad \rho_m V \quad 0.8\ \mu m^{-2} \times 1\ \mu m^3 \quad 800$ nm. Moreover, because these dislocation lines can be arbitrarily orientated, the average length of their projection on the image plane should be equal to $L/\sqrt{2} \approx 570$ nm, which fits pretty well with the two segments highlighted in Fig. 10a. Besides the low ρ_m value, an additional reason for the observation of large areas without dislocations is the lack of obstacles (hard particles) that could arrest the mobile dislocations, meaning that mobile dislocations have enough time to either annihilate

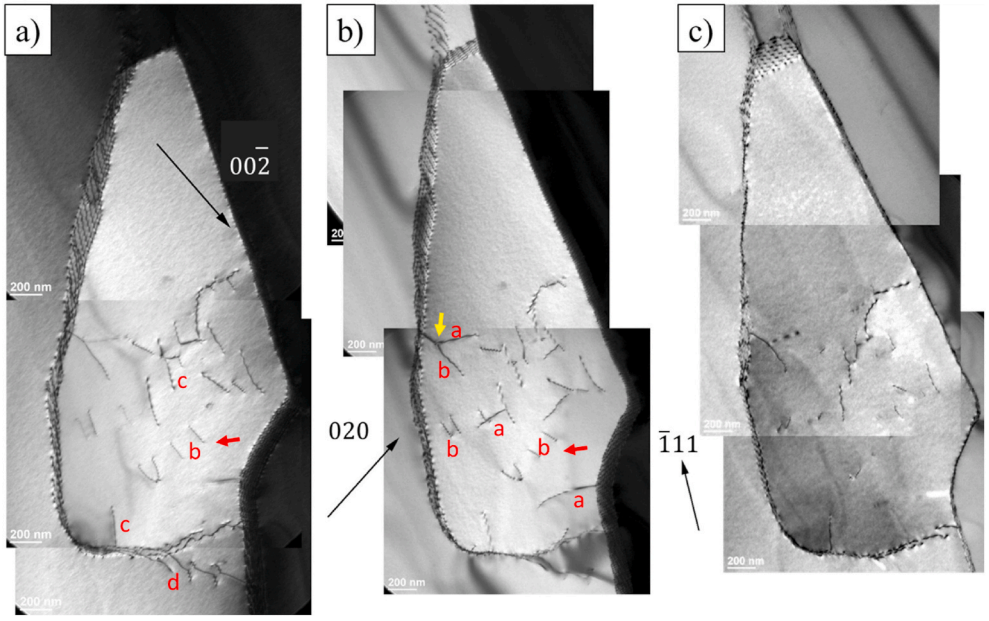

Fig. 11. Dislocations inside a subgrain in the necking area of a [001] specimen ruptured during a creep test at 1288 °C and 10 MPa. The overall creep strain is 33 % and the estimated local strain is 55 %. Bright field two-beam TEM micrographs, the diffraction vector is indicated.

Table 2
Results of the identification of the Burgers vectors of the dislocations in Fig. 11 by the invisibility criterion $(\vec{g}\cdot\vec{b})=0$.

	$\bar{2}02$	002	020	$11\bar{1}$	$\bar{1}11$	
a	✓	✗	✓	✓	✗	$a/2[110]$
b	✓	✓	✓	✗	✓	$a/2[011]$
c	✓	✓	✗	✓	✓	$a/2[10\bar{1}]$
d	✓	✓	✓	✓	✗	$a/2[0\bar{1}1]$

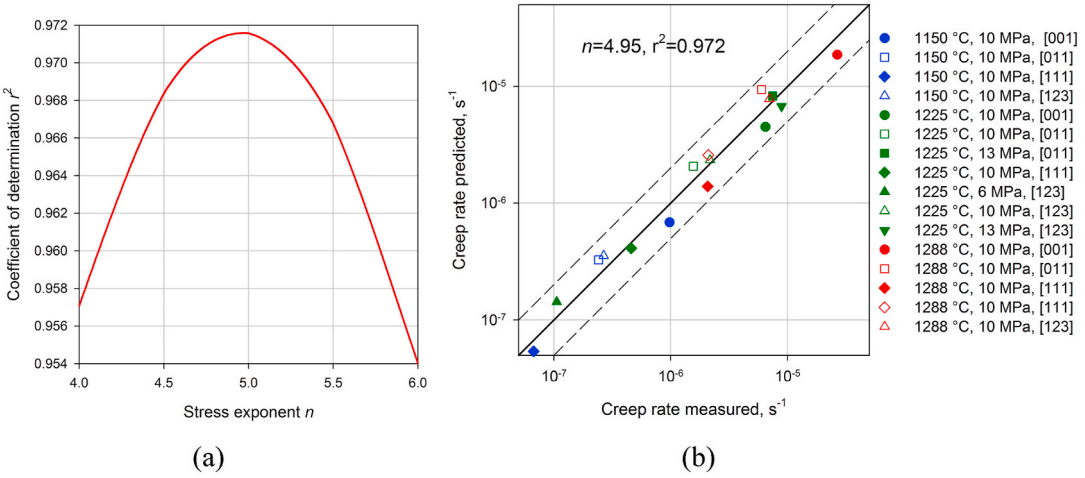

Fig. 12. Joint fitting of the creep results considering the measured specimen orientations (θ,ρ). (a) Variation of the coefficient of determination r^2 with n. (b) Comparison between measured and predicted creep rates.

Table 3
Literature data for creep of Ni-solid solutions.

Alloy	Reference	σ-range, MPa	T-range, °C	n	Q_c, kJ/mol
Ni	[23]	13–59	650–1150	5.0	276
Ni–10Cr				5.2	276
Ni–20Cr				4.6	289
Ni–25Cr				4.9	315
Ni–30Cr				4.6	307
Ni–20Cr–14Mo	[24]	49–176	800–900	5.2	415
Ni–2W	[25]	21–48	852–1005	4.8 ±	298 ± 8
Ni–4W			910–1005	0.2	311 ± 12
Ni–6W			854–1046		317 ± 8
γ-alloy	This work	6–13	1150–1288	4.95	442
Average				4.91 ± 0.18	

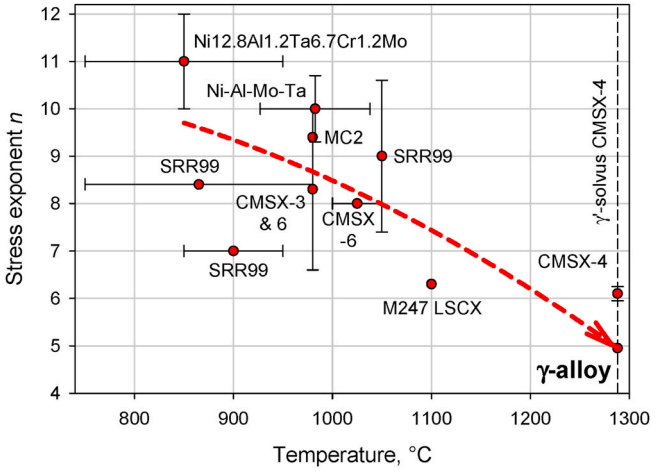

Fig. 13. Stress exponent n measured for superalloys at different temperatures (this work, [7,27]). Vertical and horizontal bars show respectively the scatter of n and the investigated temperature ranges. The dashed line shows the decreasing tendency of n with temperature.

with dislocations of opposite Burgers vector by climb or react with other dislocations, thereby rearranging in new LABs that aggregate the dislocations locally in excess (often called geometrically necessary dislocations). In this regard, it should be noticed that extinction contrast analysis performed on dislocations within the LABs has indicated that the Burgers vector of all these dislocations is of the type $a/2\langle 011\rangle$. A similar refinement of the subgrain structure during creep, leading to low energy dislocation configurations, has been often observed and regarded as a recovery mechanism in polycrystalline metals (see, e.g. Refs. [19,20]). At the high testing temperatures considered here, it is expected that these recovery mechanisms are extremely fast, hence explaining the

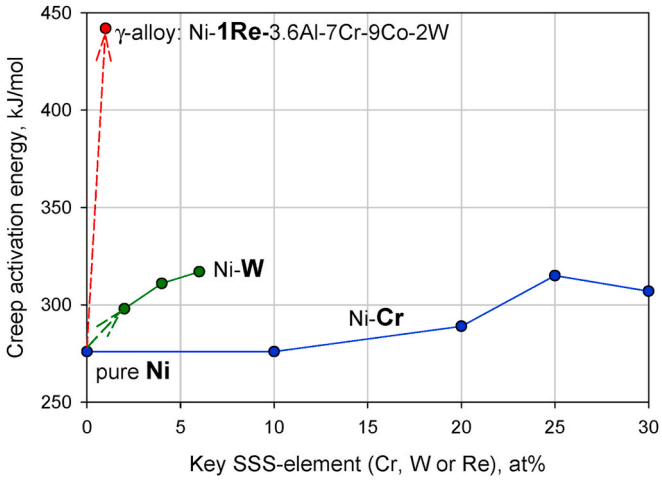

Fig. 14. Correlation of the creep activation energy Q_c with the content of the key solid solution strengthener (SSS) for different Ni-solid solutions.

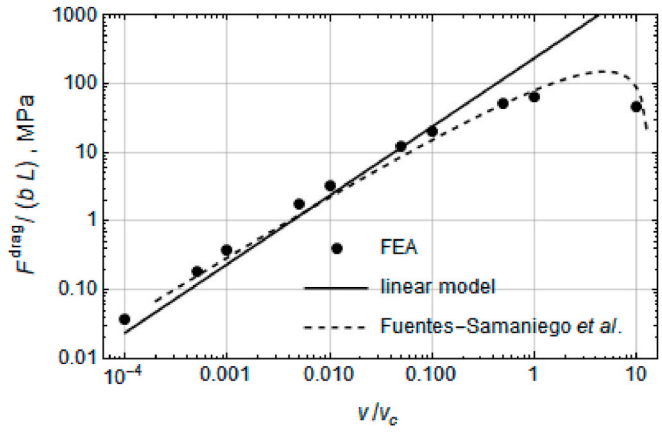

Fig. 15. Total drag force computed by FE analysis (FEA) compared to the solution [30] and linear approximation for the elements Re and W.

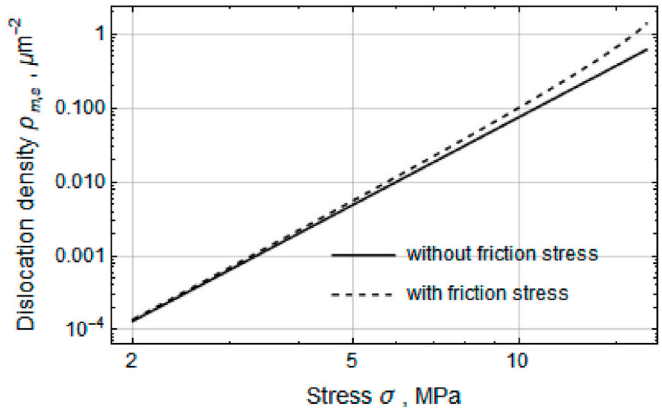

Fig. 16. Density of mobile dislocations $\rho_{m,s}$ for one slip system at 1288 °C in a [001] specimen.

existence of low dislocation density areas between the LABs in the deformed specimens.

In one instance, some dislocations inside a subgrain could be observed in the strongly deformed necking area of the [001] specimen ruptured at 1288 °C and 10 MPa, see Fig. 11. The Burgers vectors $\vec{b}$ of dislocations marked in Fig. 11 as (a, b, c, d) have been identified using the invisibility criterion $(\vec{g} \cdot \vec{b})$ 0, where $\vec{g}$ is the diffraction vector. The results are presented in Table 2. All dislocations have $a/2\langle 011\rangle$ type Burgers vectors, which confirms the activity of the usual fcc system of $\langle 011\rangle\{111\}$ octahedral slip. The dislocations marked by b, c, and d have a nonzero last index, which means that they experience an elastic force due to applied load. Most of these dislocations are obviously mobile, as for example the b-group in Fig. 11a and b (shown by red arrow), which has a typical slip band configuration. However, some dislocations have a zero last index, a priori indicating the absence of elastic force acting on these dislocations. These dislocations could have formed by reaction between mobile dislocations belonging to different slip systems, e.g., by $a/2\,[101] + a/2\,[01\bar{1}]$ $a/2\,[110]$. Such a reaction product is visible near the left subgrain border and marked by a yellow arrow in Fig. 11b. These reactions result in $a/2\,[110]$ junctions linking the dislocations and gradually knitting new LAB networks, as seen in Fig. 9d.

4. Discussion

A γ-analogue of CMSX-4 has been designed on the basis of Thermo-Calc calculations. The solidified single-crystals of this alloy have shown the same orientation dependence of the creep rate as CMSX-4 (see Fig. 5a–c) as well as the same transformation of the cross-section shape of [011] specimens (see Fig. 8), which both indicate the dominance of $\langle 011\rangle\{111\}$ octahedral slip as deformation mechanism. This result is in agreement with the widely known Weertman model for creep of solid solution alloys assuming that dislocations viscously glide under the control of solute dragging [21].

However, it has been already mentioned that the γ-alloy creeps at 1288 °C about two times faster than CMSX-4, see Fig. 5a. This lower strength could be due to a reduced content of the γ-stabilizing elements (Cr, Co, Mo) as well as total removing of the γ′-forming element Ta, see Table 1. According to Ref. [22], Ta can strengthen the γ-solid solution if its concentration is significant, which is the case of CMSX-4 at super-solvus temperatures. An additional cause for the higher creep resistance of CMSX-4 could be a small residual amount of the γ′-phase, which according to Ref. [7] still remains in the interdendritic regions of this alloy at 1288 °C. This could also be the origin of the remarkable softening of CMSX-4 during creep, which is barely distinguishable for the γ-alloy, see Fig. 6b. However, the concentration of the important elements Re and W has been kept identical to CMSX-4 and it has been verified that the creep strengths of both alloys are in the same order of magnitude. In summary, despite the mentioned differences in creep resistance, it is obvious that similar deformation mechanisms operate in both materials in the absence of the strengthening γ′-phase.

The values of the stress exponent n and the creep activated energy Q_c have been preliminarily evaluated in section 3.1 (Analysis of the creep curves) by simple linear regression of the creep rates, separately for different orientations. In the following, Q_c and n will be evaluated by a joint fitting considering all investigated orientations as well as the deviations from the ideal exact orientations measured by XRD and temperatures. This requires an analytical description of the orientation dependence of the creep rate. Such an expression was derived, e.g., in Ref. [7], for octahedral slip and a Norton power-law at the slip system level:

$$\dot{\varepsilon}_{min}(\sigma,\theta,\rho) \sim \sigma^n \Phi(\theta,\rho)$$

with

$$\Phi(\theta,\rho) \quad \sum_{s\ 1}^{12} m_s^{n+1}(\theta,\rho) \tag{1}$$

where $\dot{\varepsilon}_{min}(\sigma,\theta,\rho)$ is the minimum creep rate of a specimen, which orientation is defined by the Euler angles θ and ρ, $\Phi(\theta,\rho)$ is an orientation factor depending on θ and ρ, n is the Norton exponent and $m_s(\theta,\varrho)$

is the Schmid factor for the slip system with index s in the case of uniaxial loading along the specimen axis. Assuming an Arrhenius dependence of $\dot{\varepsilon}_{min}$ on the temperature T, one can extend Eq. (1) as follows:

$$\dot{\varepsilon}_{min}(\sigma, T, \theta, \rho) \quad A\,\sigma^{n} \quad \Phi(\theta,\rho)\exp(\quad Q_c/RT), \tag{2}$$

where A, n and Q_c are slip system independent material parameters. These parameters have been determined by maximizing the determination coefficient:

$$r^2(lA, Q_c, n) \quad 1 \quad \frac{SS_{res}}{SS_{tot}}, \tag{3}$$

where

$$SS_{res} \quad \sum_{i\ 1}^{N}\left[\ln\dot{\varepsilon}_i \quad \left(lA \quad \frac{Q_c}{RT} + n\ln\sigma + \ln\left[\sum_{j\ 1}^{12} m_{s,j}(\theta_i,\rho_i)^{n+1}\right]\right)\right]^2, \tag{4}$$

with lA $\ln A$, N is the number of tests and

$$SS_{tot} \quad \sum_{i\ 1}^{N}\left(\ln\dot{\varepsilon}_i \quad \overline{\ln\dot{\varepsilon}_i}\right)^2 \text{ with } \overline{\ln\dot{\varepsilon}_i} \quad \frac{1}{N}\sum_{i\ 1}^{N}\ln\dot{\varepsilon}_i \tag{5}$$

The maximization of $r^2(lA, Q_c, n)$ has been performed in two steps: In the first one, n is fixed, but lA and Q_c are fitted to the creep data, which corresponds to a linear regression leading to the n-dependent parameters $lA(n)$ and $Q_c(n)$. In the second step, the resulting function $r^2(n)$ has been maximized with respect to n.

The graph r^2 $f(n)$, where $1 \le n \le 10$, is shown in Fig. 12a. It is seen that r^2 $f(n)$ has only one clear maximum with $r^2 \approx 0.97$ at n 4.95. The corresponding activation energy Q_c 442 kJ/mol is within the range 430–459 kJ/mol separately determined for the different orientations, see Fig. 7a. The pre-factor A in Eq. (2) is A 3.3×10^6 $\mathrm{MPa}^{-(n+1)}\,\mathrm{s}^{-1}$.

The obtained values of n and Q_c can be compared with the results reported in the literature for Ni-solid solutions, see Table 3. For the sake of comparison, only references that do not consider a back stress (or internal stress) are presented. It is seen that n slightly varies around the average value equal to 4.91 ± 0.18, which is very close to the present result. This value is also in agreement with a statement of J. Weertman and J.R. Weertman [26]: "It is shown by experiments that for pure metals and many alloys stress exponent n 4–5". In addition, it is remarkable that the n values given in Table 3 do not correlate with the alloy composition, stress, and temperature.

Fig. 13 now shows the n-values measured for superalloys at different temperatures. These data, with the exception of CMSX-4 (our previous work [7]) and the γ-alloy (this work), are taken from Ref. [27]. Vertical and horizontal bars respectively indicate the scatter of n and the investigated temperature ranges. There is a clear tendency for the exponent n to decrease with temperature, as shown by the dashed line. At lower temperatures of about 850 °C the average of n is about 10, while at 1288 °C it is equal to 6.1 for CMSX-4 and about 5 for the γ-alloy. Obviously, this decrease of n is related to a change of the deformation mechanism due to the dissolution of the strengthening γ′-phase. When the γ′-phase totally dissolves, n should approach the typical values for Ni-solid solutions, as confirmed in the case of the γ-alloy. Note that the slightly higher exponent n previously found for CMSX-4 at 1288 °C could be also due to the small residual amount of the γ′-phase in CMSX-4, as mentioned above.

Dislocation glide can be retarded by the large solute atoms segregating at the dislocation core, as was recently [28] established by high-resolution TEM and atom probe tomography for Re in the nickel-base superalloy ERBO/1 under creep conditions. Accordingly, the dislocation velocity at high temperatures and low stresses is controlled by the diffusion mobility of these atoms, a phenomenon that has been analyzed, e.g., in Refs. [29,30]. The calculations presented in the Appendix (see Fig. 15) also confirm that the experimental stress range lies below the maximum drag force. Therefore, it is reasonable to expect that the creep activation energy Q_c of Ni-solid solutions correlates with the activation energy of diffusion Q_X^{Ni} of the solid solution strengthening (SSS) elements X in Ni. However, only a qualitative comparison is possible because of the uncertainty measurements for Q_X^{Ni}.

Fig. 14, which is based on the data from Table 3, shows the correlations between Q_c and Q_X^{Ni} for some elements contained in the γ-alloy. The horizontal scale gives the content of the key SSS-element in the considered Ni-solid solution (Cr, W or Re) and the vertical scale the corresponding creep activation energy. The value for pure Ni, Q_c 276 kJ/mol [23], is taken as a reference point. It should be noted that this value is close to the activation energy of self-diffusion in Ni, Q_{Ni}^{Ni} 278 ± 12 kJ/mol, calculated by averaging the literature data from Ref. [31]. It is seen that small Cr additions have no influence on Q_c, which agrees with the result of [32] according to which $Q_{Cr}^{Ni} \approx Q_{Ni}^{Ni}$. An increase of Q_c visible at larger Cr concentrations of 20–30 at% is not due the SSS-effect but to strengthening by the ordered intermetallic phase Ni_2Cr forming in Ni-base alloys at high Cr concentrations, see e.g. Ref. [33]. In contrast to Cr, the effect of W on Q_c is achieved at significantly lower additions. For example, an addition of 4, respectively 6 at% of W yields an increase of Q_c up to 311 ± 12, respectively 317 ± 8 kJ/mol (see Table 3). These values are close to the measurements of Q_W^{Ni}, 312 kJ/mol, and 310 ± 5 kJ/mol, respectively reported in Refs. [34,35].

However, it is seen in Fig. 14 that the γ-alloy has a much higher creep activation energy $Q_c \approx 442$ kJ/mol than the Ni–Cr and Ni–W solid solutions. According to Ref. [36], the creep resistance of the γ-matrix highly alloyed with Cr, Co, and W is raised by a factor of 20 by adding about 3 at% of Re. Therefore, it is logical to assume that the high Q_c-value found for the γ-alloy is related to the Re addition. However, due to the large uncertainty regarding the activation energy for the diffusion of Re in Ni, Q_{Re}^{Ni}, it is difficult to make a direct comparison between Q_c and Q_{Re}^{Ni}. Indeed, the values reported for Q_{Re}^{Ni} range between 196 kJ/mol and 412 kJ/mol, as discussed in Ref. [37]. The cause of this uncertainty is the extremely low diffusion mobility of Re, which makes it difficult to accurately measure Q_{Re}^{Ni}. In order to reduce this uncertainty, the theoretical estimations of the Q_{Re}^{Ni}-value could be used. According to the first-principle calculations performed by Janotti et al. [38] the dependence of the Q_X^{Ni}-value of the transition metals of 5d series on the atomic number Z has a maximum of about 337 kJ/mol at Z 75, which corresponds to Re. This value is significantly higher than that predicted for W, which is about 287 kJ/mol.

In summary, it is likely that the high creep activation energy Q_c of the γ-alloy is related to the role of Re and the high value of Q_{Re}^{Ni}. However, the question remains: why is Q_c significantly higher than Q_{Re}^{Ni}? The answer to this question requires a deeper and broader analysis, which is beyond the scope of this paper. Therefore, only two possible reasons will be noted here. First, in the γ-alloy, diffusion of Re doesn't take place in pure Ni but in the Ni-solid solution, where every fourth atom is a foreign atom. Second, the dislocation velocity and thus the creep rate are related to Q_{Re}^{Ni} through different parameters that are also temperature-dependent, e.g., the elastic constants of the alloy lattice and the volumes of solute atoms (see the appendix).

5. Conclusions

A γ-analogue of the superalloy CMSX-4 that represents the γ-solid solution of nickel at all temperatures and does not contain the strengthening γ′-phase has been designed on the base of Thermo-Calc calculations. Single crystals of this alloy of different crystallographic orientations have been tested under creep conditions in the temperature range between 1150 °C and 1288 °C.

- The tests have revealed a very high creep anisotropy of this alloy as previously observed for CMSX-4 at its supersolvus temperature of

1288 °C. This anisotropy results from the operation of ⟨011⟩{111} octahedral slip, identified as the dominant deformation mechanism. This has been confirmed by the change of the shape of [011] specimens as well as by the orientation dependence of the creep rates.

- The tests in the temperature range 1150–1288 °C yield the estimate $Q_c \cong 442$ kJ/mol of the creep activation energy, which correlates with the high activation energy of Re diffusion in Ni. This result supports the hypothesis that the motion of dislocations in the γ-matrix of Re-containing superalloys is controlled by the slow diffusion of Re atoms segregating at the dislocation core (Cottrell atmosphere). The Norton stress exponent n has been found to be equal to 5, which is a typical value for pure metals and single-phase metallic alloys.
- The absence of the γ′-reprecipitation during cooling after high-temperature creep tests facilitates microstructural investigations. It has been shown by EBSD that the creep deformation leads to an increase in the misorientations of the existing LABs. According to TEM observations, new LABs also form, which are due to reactions between the mobile $a/2\langle 011\rangle$ dislocations, leading to low energy configurations after rearrangement.

CRediT authorship contribution statement

A.I. Epishin: Conceptualization, Project administration, Writing – original draft. **B. Fedelich:** Conceptualization, Formal analysis, Writing – original draft. **B. Viguier:** Conceptualization, Investigation, Writing – original draft. **S. Schriever:** Investigation. **I.L. Svetlov:** Resources. **N.V. Petrushin:** Resources, Investigation. **R. Saillard:** Investigation. **A. Proietti:** Investigation. **D. Poquillon:** Investigation. **A. Chyrkin:** Formal analysis.

Declaration of competing interest

The authors declare that they have no known competing financial interests or personal relationships that could have appeared to influence the work reported in this paper.

Acknowledgements

This work was supported by the German Research Foundation DFG (projects Re 688/77–1 and FE 933/2–1), the French National Research Agency ANR (project ANR15-MERA-0003-04) and the Russian Foundation of Basic research (grant no. 18-508-12010). The authors also thank Prof. Robert Vaβen from the Forschungszentrum Jülich for help with protective coating of creep specimens.

Appendix. Estimates of the dislocation velocity and the density of mobile dislocations

Following e.g. Refs. [39,40], it is assumed that creep is controlled by the viscous glide of edge dislocations dragging a cloud of solute atoms (Cottrell atmosphere). The dislocation velocity v^d is then calculated under the assumption that glide is controlled by the diffusion of the large solute elements, Re and W, segregating around the dislocation core. Numerical and approximative solutions of the problem were derived for example in Refs. [29,41,42]. A rigorous analysis of the diffusion problem around the gliding dislocation was developed in the case of an infinite region in Ref. [30].

The cloud of diffusing solute atoms exerts a drag force per unit dislocation length F^{drag} $B^{drag}\, v^d$ on the gliding dislocation, where B^{drag} is the drag coefficient. The dislocation velocity results from the equilibrium condition

$$F^{drag} + F^{mech} \quad 0 \;\Rightarrow\; v^d \quad \frac{F^{mech}}{B^{drag}} \tag{6}$$

where the mechanical force corresponds to the glide component of the Peach-Kohler force, i.e., F^{mech} $b\,\tau$, in which b is the Burgers vector and τ the Resolved Shear Stress (RSS). The drag force was found to increase in a quasi-linear regime until a peak force is reached, corresponding to a critical dislocation velocity approximately equal to $v_c \cong \frac{D\,k\,T}{\beta}$ for one solute, where D is the corresponding interdiffusion coefficient and β is given by

$$\beta \quad \frac{\mu\, b}{3\,\pi}\,\frac{1+\nu}{1 \quad \nu}(\Omega_{solute} \quad \Omega_{solvent}), \tag{7}$$

where Ω_{solute} and $\Omega_{solvent}$ are the atomic volumes of the solute, respectively the solvent atoms, μ is the shear modulus, and ν is Poisson's ratio. Since the γ-alloy is compositionally close to CMSX-4 it has been assumed that $\Omega_{solvent}$ Ω_{CMSX4}. The diffusion problem for the atomic concentration c of the solutes around the moving edge dislocation has been solved by Finite Elements (FE) in a disk of radius $R_{ext} \gg b$ centered at the dislocation core and with the boundary condition $c(R_{ext})$ c_0, where c_0 is the mean atomic concentration of the solutes. Additional details are not reproduced here since similar solutions have been already presented in the literature (see e.g. Ref. [42]). In the quasi-linear regime, the drag coefficient is usually written in the form

$$B^{drag} \quad \frac{c_0\,\beta^2\,\ln(\lambda/r_0)}{\Omega\, D\, k\, T}, \tag{8}$$

where r_0 is an inner cut-off radius, λ is an outer cut-off radius, and Ω is the atomic volume of the alloy. The inner cut-off radius is usually taken of the size of the dislocation core, i.e., $r_0 \approx b$. Regarding the quantity λ, it seems that there is no universally accepted recommendation. The rigorous analysis developed in Ref. [30] for an infinite domain shows that λ is proportional to D/v for small velocities, i.e., $\frac{\beta\, v}{2\, D} \ll 1$.

The parameters entering Eqs. (7) and (8) have been chosen as follows:

The classical treatment of solute drag by a gliding edge dislocation makes use of isotropic elasticity (see e.g. Ref. [39]). Hence, the question arises of an appropriate choice of the shear modulus μ_{iso} and Poisson's ratio ν_{iso} in Eq. (7). These constants have been chosen in such a way that the pre-factor K_{cubic} contained in the energy per line unit of the straight edge dislocation $\frac{W}{L}$ $\frac{K_{cubic}\, b^2}{4\,\pi}\ln\left(\frac{R}{r_0}\right)$ of the anisotropic material matches that of the isotropic solution, i.e., $\frac{W}{L}$ $\frac{\mu_{iso}\, b^2}{4\,\pi\,(1-\nu_{iso})}\ln\left(\frac{R}{r_0}\right)$, leading to μ_{iso} K_{cubic} (1 ν_{iso}), where the expression of K_{cubic} as a function of the components of the elastic stiffness (c_{11}, c_{12}, c_{44}) is given in Ref. [41]. In addition, the bulk modulus κ_{iso} of the isotropic material is taken identical to that of the cubic material

κ_{iso} κ_{cubic} κ, leading to the second equation ν_{iso} $(3\,\kappa$ $2\,\mu_{iso})/(6\,\kappa + 2\,\mu_{iso})$. After resolution of the corresponding system of equations, the values μ_{iso} 42 GPa and ν_{iso} 0.38 are obtained for 1288 °C with the elastic constants of the γ-alloy provided in Ref. [43]. These values are also close to the Hill average of the Voigt and Reuss estimates for a polycrystal yielding to μ_{iso} 38 GPa and ν_{iso} 0.39.

The atomic volumes at Room Temperature (RT) for Re and W have been taken as Ω_{Re} 1.47×10^{-29} m^3 and Ω_W 1.57×10^{-29} m^3 [44]. The lattice spacing for CMSX-4 at RT [45] has been taken as a 3.6×10^{-10} m, which leads to the atomic volume of the alloy Ω $\Omega_{solvent}$ 1.16×10^{-29} m^3. Estimates of the atomic volumes $\Omega(T)$ at high temperature have been obtained by applying the linear thermal dilatation coefficients $\alpha(T)$ $\frac{\Delta L}{L_0}$, that is $\Omega(T)$ $\Omega_0\,(1 + \alpha(T))^3$. The thermal dilatation for Re

$$\alpha(T) \quad 9.7910^{\ 5} + 5.8910^{\ 6}\,T + 8.5710^{\ 10}T^2, \tag{9}$$

with T in °C has been taken from Ref. [46]. The thermal dilatation for W

$$\alpha(T) \quad 1.389610^{\ 3} \quad 8.279710^{\ 7}T + 4.055710^{\ 9}\,T^2 \quad 1.216410^{\ 12}\,T^3 + 1.703410^{\ 16}T^4, \tag{10}$$

with T in K has been taken from [47]. For the γ-alloy, the thermal dilatation determined for CMSX-4 reported in Ref. [43] has been used.

The interdiffusion coefficients for Re and W in the γ-alloy are not known as mentioned above. For an estimate, the coefficients for interdiffusion in pure Ni are considered. For Re, this coefficient is given in Ref. [37] in the form

$$D_{Re} \quad D_{Re,0}\,\exp\left(\quad \frac{Q_{Re}}{R\,T}\right) \tag{11}$$

where $D_{Re,0}$ 1.2×10^{-4} m^2/s and Q_{Re} 317 kJ /mol. At 1288 °C, D_{Re} 2.9×10^{-15} m^2/s. For W it is given in Ref. [35] as

$$D_W \quad D_{W,0}\,\exp\left(\quad \frac{Q_W}{R\,T}\right) \tag{12}$$

where $D_{W,0}$ 2.5×10^{-4} m^2/s and Q_W 310 kJ /mol. At 1288 °C, D_W 1.1×10^{-14} m^2/s.

In the case of two species (Re and W), the total drag force is the sum of the contributions of both species, and we can write F^{drag} $F_W^{drag} + F_{Re}^{drag}$. In accordance, the total drag coefficient is

$$B^{drag} \quad B_W^{drag} + B_{Re}^{drag} \quad \frac{\ln(\lambda/r_0)}{\Omega\ \ k\,T}\left(\frac{c_{W,0}\,\beta_W^2}{D_W} + \frac{c_{Re,0}\,\beta_{Re}^2}{D_{Re}}\right) \tag{13}$$

where the atomic concentrations $c_{W,0}$ and $c_{Re,0}$ are indicated in Table 1 for the γ-alloy. For comparison with the applied stress levels, the total drag force F^{drag} per unit line is divided by the Burgers vector and plotted in Fig. 15. The FE solution agrees well with that derived by Fuentes-Samaniego et al. in Ref. [30]. It follows from this analysis that at the stress levels of the creep tests the dislocation motion is within the range of control by solute diffusion with the dislocation core.

It can be also seen that the quasi-linear regime applies at RSS below 10 MPa. In this range, with the value $\ln(\lambda\,/r_0)$ 3, the linear model matches the FE results. For example, at T 1288 °C, we obtain B^{drag} 3.7 kN/m^{-2} s.

Finally, for the slip system s, the density of mobile dislocations $\rho_{m,s}$ can be inferred from the Orowan relation $\dot{\gamma}_s$ $b\,\rho_{m,s}\,v_s$ $b^2\,\rho_{m,s}\,\tau_s/\,B^{drag}$, where $\tau_g$is the resolved shear stress. In the case of a [001] specimen, the previous equation can be rewritten for the minimum creep rate

$$\rho_{m,s} \quad \frac{B^{drag}\,\dot{\varepsilon}_{min}}{8\,m_{001}^2\,b^2\,\sigma} \tag{14}$$

where m_{001} 0.41 is the Schmid factor in the direction [001]. A power-law of [fx] with an exponent n 1 is thus obtained for $\rho_{m,s}$. Note that the previous Eq. doesn't account for internal stresses. A friction stress of the type τ_c $\alpha\,\mu\,b\,\sqrt{\rho_{m,s}}$ following Taylor's model can be accounted for, which amounts to replace τ_s $m_{001}\,\sigma$ by $m_{001}\,\sigma$ τ_c in Eq. (14). Thereby, the numerical factor α is usually taken as $\alpha \approx 0.3$. In accordance, $\rho_{m,s}$ is found by solving the equation

$$\rho_{m,s} \quad \frac{B^{drag}\,\dot{\varepsilon}_{min}}{8\,m_{001}\,b^2\left(m_{001}\,\sigma \quad \alpha\,\mu\,b\,\sqrt{\rho_{m,s}}\right)} \tag{15}$$

The densities $\rho_{m,s}$ estimated with the identified creep law (1) for both estimates (14) and (15) are plotted at 1288 °C in Fig. 16. In the considered stress range, the friction stress has only a limited influence. For 10 MPa, the density of mobile dislocations $\rho_{m,s}$ in each slip system of a [001] specimen is equal to about 0.1 μm^{-2}. Thus, the total mobile dislocation density for all 8 active slip systems is

ρ_m $0.1 \times 8 \approx 0.8{\cdot}\mu\text{m}^{\ 2}$

Data availability statement

The data that support the findings of this study are available on request from the corresponding author (BF).

References

[1] L.G. Fritzemeier, The influence of high thermal gradient casting, hot isostatic pressing and alternative heat treatment on the structure and properties of a single crystal nickel base superalloy, in: S. Reichman, D. Duhl, G. Maurer, S. Antolovich, C. Lund (Eds.), Superalloys 1988, TMS, Warrendale, 1988, pp. 265–274, https://doi.org/10.7449/1988/superalloys_1988_265_274.

[2] K.P.L. Fullagar, R.W. Broomfield, M. Hulands, K. Harris, G.L. Erickson, S. L. Sikkenga, Aero engine test experience with CMSX-4 alloy single-crystal turbine blades, J. Eng. Gas Turbines Power 118 (1996) 380–388, https://doi.org/10.1115/1.2816600.

[3] A. Epishin, B. Fedelich, T. Link, T. Feldmann, I.L. Svetlov, Pore annihilation in a single-crystal nickel-base superalloy during hot isostatic pressing: experiment and modelling, Mater. Sci. Eng. A 586 (2013) 342–349, https://doi.org/10.1016/J.MSEA.2013.08.034.

[4] A.I. Epishin, T. Link, B. Fedelich, I.L. Svetlov, E.R. Golubovskiy, Hot isostatic pressing of single-crystal nickel-base superalloys: mechanism of pore closure and effect on mechanical properties, MATEC Web of Conferences 14 (2014), 088003, https://doi.org/10.1051/matecconf/20141408003.

[5] L. Mujica Roncery, I. Lopez-Galilea, B. Ruttert, S. Huth, W. Theisen, Influence of temperature, pressure, and cooling rate during hot isostatic pressing on the microstructure of an SX Ni-base superalloy, Mater. Des. 97 (2016) 544–552, https://doi.org/10.1016/j.matdes.2016.02.051.

[6] R.E. Shalin, I.L. Svetlov, E.B. Kachanov, V.N. Toloraja, O.S. Gavrilin, Single Crystals of Nickel-Base Superalloys, Mashinostroenie, Moscow, 1997.

[7] A.I. Epishin, B. Fedelich, G. Nolze, S. Schriever, T. Feldmann, M.F. Ijaz, B. Viguier, D. Poquillon, Y. Le Bouar, A. Ruffini, A. Finel, Creep of single crystals of nickel-based superalloys at ultra-high homologous temperature, Metall. Mater. Trans. 49 (2018) 3973–3987, https://doi.org/10.1007/s11661-018-4729-6.

[8] K. Harris, G.L. Erickson, S.L. Sikkenga, W.D. Brentnall, J.M. Aurrecoechea, K. G. Kubarych, Development of the rhenium containing superalloys CMSX-4 & CM 186 LC for single crystal blade and directionally solidified vane applications in advanced turbine engines, J. Mater. Eng. Perform. 2 (4) (1993) 481–487, https://doi.org/10.1007/BF02661730.

[9] J.O. Andersson, T. Helander, L. Hoglund, P. Shi, B. Sundman, Thermo-calc & dictra, computational tools for materials science, Calphad 26 (2002) 273–312, https://doi.org/10.1016/S0364-5916(02)00037-8.

[10] T.T. TTNi7, Ni-based Superalloys Database in, 2006.

[11] V. Sass, M. Feller-Kniepmeier, Orientation dependence of dislocation structures and deformation mechanisms in creep deformed CMSX-4 single crystals, Mater. Sci. Eng. A 245 (1998) 19–28, https://doi.org/10.1016/S0921-5093(97)00709-0.

[12] D. Bettge, W. Osterle, "Cube slip" in near-[111] oriented specimens of a single-crystal nickel-base superalloy, Scripta Mater. 40 (1999) 389–395, https://doi.org/10.1016/S1359-6462(98)00446-1.

[13] S.D. Mesarovic, Dislocation creep: climb and glide in the lattice continuum, Crystals 7 (2017) 243, https://doi.org/10.3390/cryst7080243.

[14] R. S Barnes, The climb of edge dislocations in face-centred cubic crystals, Acta Metall. 2 (1954) 380–385, https://doi.org/10.1016/0001-6160(54)90055-3.

[15] A. Abu-Odeh, M. Cottura, M. Asta, Insights into dislocation climb efficiency in FCC metals from atomistic simulations, Acta Mater. 193 (2020) 172–181, https://doi.org/10.1016/j.actamat.2020.04.047.

[16] F.R.N. Nabarro, Deformation of crystals by the motion of single ions, in: N.F. Mott (Ed.), Report of a Conference on Strength of Solids, Physical Society, London, 1948, pp. 75–90.

[17] C. Herring, Diffusional viscosity of a polycrystalline solid, J. Appl. Phys. 21 (1950) 437–445, https://doi.org/10.1063/1.1699681.

[18] U. Brückner, A. Epishin, T. Link, Local X-ray diffraction analysis of the structure of dendrites in single-crystal nickel-base superalloys, Acta Mater. 45 (1997) 5223–5231, https://doi.org/10.1016/S1359-6454(97)00163-8.

[19] M.E. Kassner, Fundamentals of Creep in Metals and Alloys, second ed., Elsevier, Amsterdam, 2009.

[20] W. Blum, P. Eisenlohr, Dislocation mechanics of creep, Mater. Sci. Eng. A (2009) 7–13, https://doi.org/10.1016/j.msea.2008.04.110, 510–511.

[21] J.-S. Zhang, High Temperature Deformation and Fracture of Materials, Chapter 5.4.1 Weertman Model, WP Science Press, 2010, pp. 78–79, https://doi.org/10.1016/B978-0-85709-079-9.50028-8.

[22] H. Rehman, K. Durst, S. Neumeier, A. Sato, R. Reed, M. Goken, On the temperature dependent strengthening of nickel by transition metal solutes, Acta Mater. 137 (2017) 54–63, https://doi.org/10.1016/j.actamat.2017.05.038.

[23] K. Monma, H. Suto, H. Oikawa, High-temperature creep of nickel-chromium alloys (On the relation between high-temperature creep and diffusion in nickel base solid solutions, IV), J. Japan Inst. Metals 28 (1964) 253–258, https://doi.org/10.2320/jinstmet1952.28.5_253.

[24] L.M. Nerodenko, E.V. Dabizha, Comparative analysis of high-temperature creep parameters of nickel and solid solutions Ni-20 Cr and Ni-20 Cr-14Mo, Strength Mater. 11 (1979) 375–379, https://doi.org/10.1007/BF00767685.

[25] W.R. Johnson, C.R. Barrett, W.D. Nix, The high-temperature creep behavior of Nickel-rich Ni-W solid solutions, Metall. Trans. 3 (1972) 963–969, https://doi.org/10.1007/BF02647673.

[26] J. Weertman, J.R. Weertman, Mechanical properties, strongly temperature dependent, in: R.W. Cahn, P. Haasen (Eds.), Physical Metallurgy, Part 2, third ed., North-Holland Phys. Publ., Amsterdam, 1983, pp. 1309–1340, https://doi.org/10.1002/crat.2170200229.

[27] P. Wollgramm, H. Buck, K. Neuking, A.B. Parsa, S. Schuwalow, J. Rogal, R. Drautz, G. Eggeler, On the role of Re in the stress and temperature dependence of creep of Ni-base single crystal superalloys, Mater. Sci. Eng. A 628 (2015) 382–395, https://doi.org/10.1016/j.msea.2015.01.010.

[28] X. Wu, S.K. Makineni, C.H. Liebscher, G. Dehm, J.R. Mianroodi, P. Shanthraj, B. Svendsen, D. Bürger, G. Eggeler, D. Raabe, B. Gault, Unveiling the Re effect in Ni-based single crystal superalloys, Nat. Commun. 11 (2020) 389, https://doi.org/10.1038/s41467-019-14062-9.

[29] S. Takeuchi, A.S. Argon, Glide and climb resistance to the motion of an edge dislocation due to dragging a cottrell atmosphere, Philos. Mag. A 40 (1979) 65–75, https://doi.org/10.1080/01418617908234833.

[30] R. Fuentes-Samaniego, R. Gasca-Neri, J.P. Hirth, Solute drag on moving edge dislocations, Philos. Mag. A A49 (1984) 31–43, https://doi.org/10.1080/01418618408233426.

[31] J.R. MacEwan, J.U. MacEwan, L. Yaffe, Self-diffusion in polycrystalline nickel, Can, J. Chem. 37 (1959) 1623–1628, https://doi.org/10.1139/v59-236.

[32] A. Engstrom, J. Ågren, Assessment of diffusional mobilities in face-centered cubic Ni-Cr-Al Alloys, Z. Metallkd. 87 (1996) 92–97, https://doi.org/10.1515/ijmr-1996-870205.

[33] Å. Martinsson, Aging Influence on Nickel-Based Superalloys at Intermediate Temperatures (400-600 °C), Luleå University of Technology, Luleå, Schweden, 2006. https://www.diva-portal.org/smash/get/diva2:1022216/FULLTEXT01.pdf.

[34] M.S.A. Karunaratne, P. Cater, R.C. Reed, Modelling of the micro-segregation in CMSX-4 superalloy and its homogenization during heat treatment, in: T. M Pollock, R. D Kissinger, R.R. Bowman, K.A. Green, M. McLean, S. Olson, J.J. Schirra (Eds.), Superalloys 2000, TMS, Warrendale, 2000, pp. 263–272, https://doi.org/10.7449/2000/Superalloys_2000_263_272.

[35] A.I. Epishin, T. Link, G. Noltze, I.L. Svetlov, B.S. Bokshtein, A.O. Rodin, R. S. Neumann, G. Oder, Diffusion processes in multicomponent nickel-base superalloy-nickel system, Phys. Met. Metallogr. 115 (2014) 21–29, https://doi.org/10.1134/S0031918X14010050.

[36] E. Fleischmann, C. Konrad, J. Preußner, R. Volkl, E. Affeldt, U. Glatzel, Influence of solid solution hardening on creep properties of single-crystal nickel-based superalloys, Metall. Mater. Trans. 46 (2015) 1125–1130, https://doi.org/10.1007/s11661-014-2727-x.

[37] A.I. Epishin, A.O. Rodin, B.S. Bokshtein, G. Oder, T. Link, I.L. Svetlov, Interdiffusion in binary Ni-Re alloys, Phys. Met. Metallogr. 116 (2015) 175–181, https://doi.org/10.1134/S0031918X15020131.

[38] A. Janotti, M. Krčmar, C.L. Fu, R.C. Reed, Solute diffusion in metals: larger atoms can move faster, Phys. Rev. Lett. 92 (2004), https://doi.org/10.1103/PhysRevLett.92.085901, 085901-1-085901-4.

[39] W. Blum, P. Eisenlohr, F. Breutinger, Understanding creep-a review, Met. Mat. Trans. A33 (2001) 291–303, https://doi.org/10.1007/s11661-002-0090-9.

[40] S. Takeuchi, A.S. Argon, Steady-state creep of alloys due to viscous motion of dislocations, Acta Metall. 24 (1976) 883–889, https://doi.org/10.1016/0001-6160(76)90036-5.

[41] J.P. Hirth, J. Lothe, Theory of Dislocations, second ed., John Wiley & Sons, New-York, 1982.

[42] M. Sakamoto, Diffusion equation and Cottrell atmosphere dragging of edge dislocation in high concentration solid solutions, Mater. Trans., JIM 30 (1989) 337–344, https://doi.org/10.2320/matertrans1989.30.337.

[43] A.I. Epishin, B. Fedelich, M. Finn, G. Künecke, B. Rehmer, G. Nolze, C. Leistner, N. Petrushin, I. Svetlov, Investigation of elastic properties of the single-crystal nickel-base superalloy CMSX-4 in the temperature interval between Room temperature and 1300 °C, Crystals 11 (2021) 152, https://doi.org/10.3390/cryst11020152.

[44] C.N. Singman, Atomic volume and allotropy of the elements, J. Chem. Educ. 61 (1984) 137–142, https://doi.org/10.1021/ed061p137.

[45] A. Epishin, U. Brückner, P.D. Portella, T. Link, Influence of small rhenium additions on the lattice spacing of nickel solid solution, Scripta Mater. 48 (2003) 455–459, https://doi.org/10.1016/S1359-6462(02)00436-0.

[46] J.B. Conway, Properties of Some Refractory Metals. Part III: Thermal Expansion Characteristics of Tungsten, Rhenium, Tantalum, Molybdenum, Niobium, W-25Re, Ta-10W, and Mo-50Re. Technical Report Nr, GEMP-375 of the General Electric Co., 1965, https://doi.org/10.2172/4617210.

[47] A.P. Müller, A. Cezairliyan, Thermal expansion of tungsten in the range 1500-3600 K by a transient interferometric technique, Int. J. Thermophys. 11 (1990) 619–628, https://doi.org/10.1007/BF01184332.